Titre: Title:	Enhanced determination of emission fine structure and orientation of individual quantum dots based on correction algorithm for spectral diffusion. Supplément
Auteurs: Authors:	Pascal Gumbsheimer, Frieder Conradt, Yannic Behovits, Steffen Huber, Christopher Hinz, Carla Negele, Stefan Mecking, Denis Seletskiy, & Alfred Leitenstorfer
Date:	2021
Type:	Article de revue / Article
Référence: Citation:	Gumbsheimer, P., Conradt, F., Behovits, Y., Huber, S., Hinz, C., Negele, C., Mecking, S., Seletskiy, D., & Leitenstorfer, A. (2021). Enhanced determination of emission fine structure and orientation of individual quantum dots based on correction algorithm for spectral diffusion. Journal of Physics D: Applied Physics, 54(15), 155106 (10 pages). https://doi.org/10.1088/1361-6463/abda83

Titre de la revue: Journal Title:	Journal of Physics D: Applied Physics (vol. 54, no. 15)
Maison d'édition: Publisher:	IOP Publishing
URL officiel: Official URL:	https://doi.org/10.1088/1361-6463/abda83
Mention légale: Legal notice:	

Supplementary Material

Enhanced Determination of Emission Fine Structure and Orientation of Individual Quantum Dots Based on Correction Algorithm for Spectral Diffusion

Pascal Gumbsheimer, Frieder Conradt, Yannic Behovits, Steffen Huber, Christopher Hinz, Carla Negele, Stefan Mecking, Denis V. Seletskiy, and Alfred Leitenstorfer

1. Assignment of quantum states to fine-structure lines

For nearly spherical colloidal quantum dots in wurtzite structure and a core radius of $R_{CdSe} \approx 2$ nm, it is well known that the energetic lowest state is the $m_F = \pm 2$ state which corresponds to transition *F* [1], followed by the state ±1L corresponding to the *A* transitions. The next bright state in increasing order is the ±1U state. For relatively spherical quantum dots, it is located tens of meV higher than the bandedge states ±2 and ±1L [2]. At this point, we emphasize the high uniformity and symmetry of our QDs [3], which are verified by TEM micrographs [4]. Due to this energetic distance and the resulting minor state occupation at cryogenic temperatures, the ±1U does not contribute to the emission fine structure. Consequently, only the ±2 and the ±1L states determine the observed QD fine structure.

Furthermore, the slight asymmetry of the confinement potential in the a-b plane of the wurtzite structure results in a lifted degeneracy of the ±1L ($m_F = \pm 1$) state in our sample, resulting in the ground state transitions A_1 and A_2, which we observe at an energetic position of a few meV above the F transition [5].

Experimentally, our assignment is supported by measurements in an external magnetic field. As an example, we analyze the photoluminescence of a single colloidal quantum dot in a varying magnetic field of up to 5 T. Ascribing the states $|A_1\rangle$ and $|A_2\rangle$ e.g. to ±1L and ±1U, respectively,

one would expect an intrinsic Zeeman splitting of these states as well. Due to difference in magnetic quantum number ($m_F = \pm 1$ instead of $m_F = \pm 2$), the splitting of the contributing states would be weaker but clearly resolvable with our apparatus. Consequently, we can safely exclude a contribution of the ±1U states to our photoluminescence signals. Instead, the analysis in Fig. S1 shows that our results fit perfectly to the assumption of a degenerate F and intrinsically split A_1 and A_2 states.

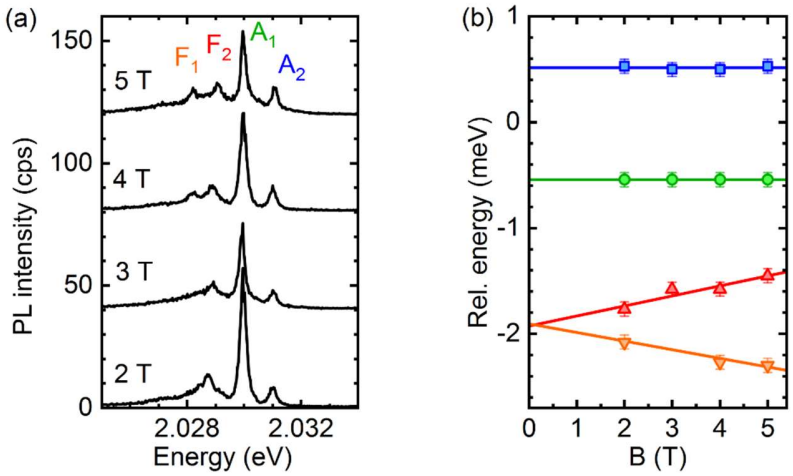

Figure S1. (a) Photoluminescence spectra of a typical QD from our sample for varying magnetic fields of up to 5 T. (b) Extracted energetic positions of the emission lines F_1, F_2, A_1 and A_2. Solid lines with the same color coding are least-square fits to the data based on the described model [6].

Finally, we want to mention that also the attribution of lines to discrete acoustic phonon sidebands can be ruled out, as supported by a multitude of arguments. Especially, the magnetic field measurements in Fig. S1 show a splitting of the dipole-forbidden line while the behavior of the higher states is totally different. This finding excludes the state $|F\rangle$ to be a phonon replica of the states found at higher energies. Note that both acoustic and optical phonon replica are visible in Fig. 2(c) of our manuscript. The amplitude of these lines is significantly smaller than the zero-phonon lines analyzed in the present work.

2. Performance of the shifting algorithm

The presented correction method relies on a very accurate and robust algorithm to determine the spectral shift of each single PL spectrum. When SNR reaches critically low values, this process becomes increasingly ambitious. In order to reduce the uncertainty of the determination of spectral positions, we use the cross-correlation between every spectrum with a reference spectrum (see main text, here k=54 is the reference spectrum) as guidance. This reference spectrum ("lucky shot") is the spectrum least distorted by noise, thus representing the reality in the best way available. To identify this spectrum, we use a mathematical measure D_k, comparing different

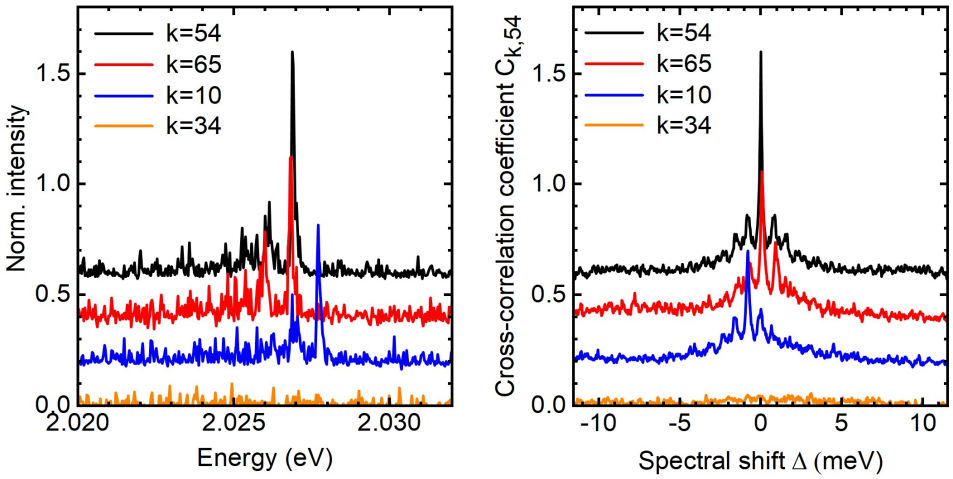

Figure S2. (left) Four selected PL spectra of a single quantum dot. The data were deliberately taken with very short integration times, resulting in a reduced SNR. (right) Correlation values as function of the spectral shift Δ of the four spectra with the black spectrum (k=54). A clear improvement of the SNR due to the correlation algorithm is clearly discernible. This fact results in a much higher accuracy for the spectral correction as compared to e.g., a shifting based only on the raw data.

spectra to determine the spectrum with the highest similarity to all the other spectra. This task is carried out by a cross-correlation step including the best spectral shift. The determination of the lucky shot can be performed based on the valuable assumption that the acquired noise is

uncorrelated whereas the underlying PL signal is identical in every spectrum, which is guaranteed by the high frequencies of acquisition in comparison to the frequencies of discrete energetic shifting events for the majority of spectra. The comparison of every spectrum k with another spectrum j out of all n spectra results in n correlation coefficients $C_{k,j}$. Adding up all these values results in D_k (see also main text).

This reference spectrum allows the exact determination of the spectral shift of every single spectrum which contains uncorrelated noise and a certain amount of information given by the PL signal. As one can see in the left part of Fig. S2, the fine-structure lines appear with a similar pattern. Therefore, the values of an additional cross-correlation step of two spectra as a function of the energetic shift between those spectra show a clear maximum when the PL signatures are placed on the same spectral position (Fig. S2, right). Note the reduced noise given by this evaluation technique (also in the case of k=34 without any PL signal). We use this method to obtain the spectral position and to rate the quality of each spectrum. After a final integration step, a consequent selection of the best spectra and an energetic shift results in a corrected spectrum. It features the fine structure of the PL emission since every single noised spectrum contains this information. Therefore, integration times of single spectra must be short enough to keep the probability of spectral shifts during the acquisition time minimal. To determine the necessary SNR

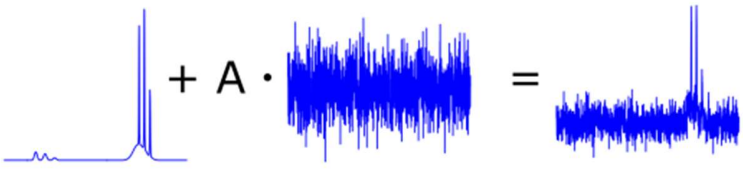

Figure S3. Data preparation with ideal PL spectrum and random noise.

of the single measured spectra to reconstruct the fine structure, we created a collection of benchmark datasets of 1000 single spectra with a well-defined SNR. Each spectrum consists of a

noise-free PL spectrum (multiple Gaussian functions) on which we add a certain amount of noise (factor A, see Fig. S3) and an additional spectral shift.

Knowing exactly the spectral shift added to each single spectrum, we can then create the average spectrum of the perfectly backshifted dataset to obtain the best possible result for the presented case. Figure S4 shows examples of three cases differing in the SNR of the single spectra.

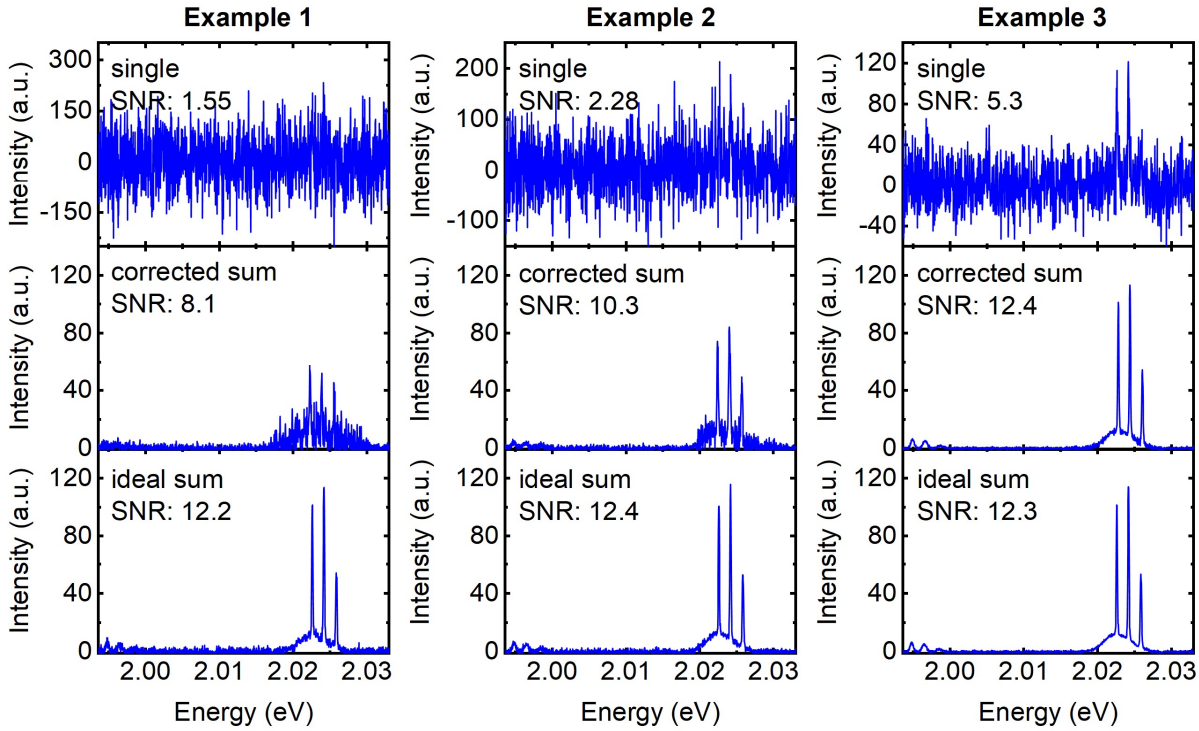

Figure S4. Three examples of different SNR of the input data (top row/single spectrum). A set of 1000 spectra with comparable SNR processed by our correction method results in the spectra shown in the center (corrected sum). As a reference, the best possible spectrum with zero shift is shown at the bottom, respectively (ideal sum).

The top row of the graphs shows a single spectrum of each set. The respective SNR is exactly known as the spectral series have been created as described above. For each of all 1000 spectra, the random energetic shift has been evaluated and corrected by our correlation method. A final integration step leads to the corrected spectra in the central row. The spectra in the lower row can

be taken as reference for the best possible spectrum that can be obtained by each data set. Please note that even for the lowest quality of the input signal with a SNR = 1.55, the fine-structure splitting is recovered. At an input SNR of 5.3, the PL spectrum is almost perfectly reconstructed. To benchmark the quality of the obtained spectra, we repeated this procedure with 200 different input SNRs in the range from 0.5 to 6.

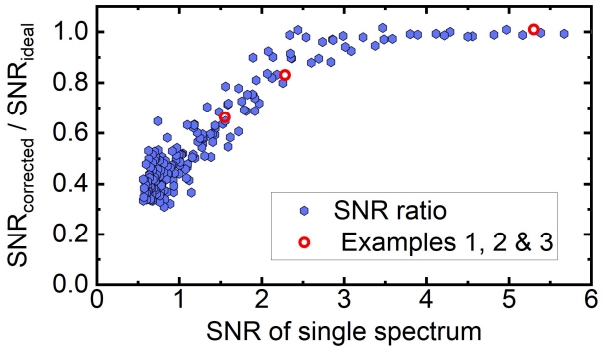

Figure S5. Ratio of the SNR obtained from corrected spectra as compared to the ideal spectra which would result if the amount of spectral shift for each one would be known depicted versus the SNR of a single input spectrum.

To quantify the success of reconstruction, we calculate the ratio of SNRs of the spectrum obtained by the correction method and the best possible spectrum ($SNR_{corrected}$ / SNR_{ideal}). When this ratio is close to one, the lowest possible SNR when processing the raw data has been reached indicating a highly successful reconstruction of the original PL spectrum. This ratio is then plotted as a function of the input SNR of a single spectrum. The results are depicted in Fig. S5. The examples shown in Fig. S4 are represented as red circles. As soon as the input SNR exceeds a value of 2, the ratio approaches unity and a highly reliable result of the corrected data is expected.

3. Error analysis for the determination of orientation angles

The error margins ϕ_{err} and θ_{err} of the orientation-defining angles ϕ and θ are depicted in Fig. S6 (a) and (b), respectively.

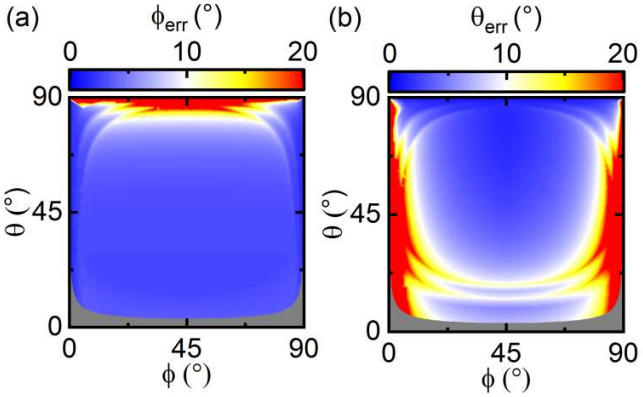

Figure S6. Calculated error margins ϕ_{err} (a) and θ_{err} (b) color-coded as a function of the orientation-defining angles ϕ and θ of a QD. This example is based on a realistic case of experimental errors for the phase differences $\Delta\alpha_i$ of $\pm$ 2°. The majority of points in the (ϕ, θ) plane supports stable solutions with ϕ_{err} and θ_{err} with a maximal error amplitude below 20°.

The statistical error in all three relevant phase differences $\Delta\alpha_i$ is typically better than $\pm$ 2°. These values are limited by spectral diffusion and the resulting slight modulation of emitted intensity [3]. To estimate the error margins, we use Eq. (7) of the main text linking the relative phases to the orientation-defining angles ϕ and θ. The uncertainties ϕ_{err} and θ_{err} are calculated by a linear sampling with n points around the relevant $\Delta\alpha_i$ up to $\pm$ 2°. Numerical inversion of Eq. (7) leads to $3n$ (one n for $\Delta\alpha(\mathrm{A}_1, \mathrm{F})$, $\Delta\alpha(F, A_2)$ and $\Delta\alpha(A_1, A_2)$, respectively) different relations in (ϕ, θ) space. Searching all intersections of pairs of these 3n relations finally results in $3n^2$ intersection points. Finding the intersection points with the highest deviation in ϕ and θ with respect to the orientation defined by the three values α_i leads to ϕ_{err} and θ_{err}. Practically, this procedure results in a rather conservative estimate for the errors. The symmetric behavior in ϕ is caused by the assumption of the same error magnitude of all α_i. The grey-shaded areas represent instabilities during the searching process for determining the intersection points. The majority of the maximal

error amplitudes ϕ_{err} and θ_{err} are far below 20°. Due to the nonlinear dependence of ϕ and θ on the relative phases, relatively high error amplitudes occur at extreme angles of ϕ below 10.0° and above 80.0° and for θ above 85°, respectively. In these cases, a maximally exact determination of relative phases necessitates an extended integration time.

[1] Efros A L, Rosen M, Kuno M, Nirmal M, Norris D and Bawendi M 1996 Band-edge exciton in quantum dots of semiconductors with a degenerate valence band: Dark and bright exciton states *Phys. Rev. B* **54** 4843–56

[2] Fernée M J, Tamarat P and Lounis B 2013 Cryogenic single-nanocrystal spectroscopy: Reading the spectral fingerprint of individual CdSe quantum dots *J. Phys. Chem. Lett.* **4** 609–18

[3] Negele C, Haase J, Budweg A, Leitenstorfer A and Mecking S 2013 Stable single-photon emission by quantum dot/polymer hybrid particles *Macromol. Rapid Commun.* **34** 1145–50

[4] Werschler F, Hinz C, Froning F, Gumbsheimer P, Haase J, Negele C, De Roo T, Mecking S, Leitenstorfer A and Seletskiy D V. 2016 Coupling of Excitons and Discrete Acoustic Phonons in Vibrationally Isolated Quantum Emitters *Nano Lett.* **16** 5861–5

[5] Htoon H, Furis M, Crooker S A, Jeong S and Klimov V I 2008 Linearly polarized “fine structure” of the bright exciton state in individual CdSe nanocrystal quantum dots *Phys. Rev. B* **77** 35328

[6] Bayer M, Ortner G, Stern O, Kuther A, Gorbunov A A, Forchel A, Hawrylak P, Fafard S, Hinzer K, Reinecke T L, Walck S N, Reithmaier J P, Klopf F and Schäfer F 2002 Fine structure of neutral and charged excitons in self-assembled In(Ga)As/(Al) GaAs quantum dots *Phys. Rev. B* **65** 195315